Sound energy harvesting by leveraging a 3D-printed phononic crystal lens

Ahmed Allam, Karim Sabra, and Alper Erturk[a)]
G. W. Woodruff School of Mechanical Engineering, Georgia Institute of Technology, Atlanta, Georgia 30332, USA

(Dated: 10 August 2021)

We investigate the harvesting of sound waves by exploiting a 3D-printed gradient-index phononic crystal lens. The concept is demonstrated numerically and experimentally for focusing audio frequency range acoustic waves in air to enhance sound energy harvesting. A finite-element model is developed to design the unit cell dispersion properties and to construct the 3D lens for wave field simulations. Numerical simulations are presented to confirm the focusing of incident plane waves and to study the sensitivity of the refractive index profile to the direction of wave propagation. The theoretical predictions are validated experimentally using a scanning microphone setup under speaker excitation, and a very good agreement is observed between the experimental and numerical wave fields. A circular piezoelectric unimorph harvester is placed at the focal position of the lens, and its performance is characterized with a resistor sweep in the absence and presence of the lens, resulting in more than an order of magnitude enhancement in the harvested power with the lens. The 3D-printed lens presented here substantially enhances the intensity of sound energy via focusing, yielding micro-Watt level power output, which can find applications for wireless sensors and other low-power electronic components.

Acoustic energy harvesting has received growing attention as a potential way of powering small electronic devices such as ultra low power sensors. Various transduction mechanisms, such as electromagnetic and piezoelectric techniques, have been used to convert acoustic waves into usable electric power toward powering wireless sensors by eliminating battery replacement[1–3]. While audio frequency acoustic waves, i.e. sound waves, are abundantly available in everyday life, they exhibit a low power density, which has limited the power harvested from air-borne sound mostly to nano-Watt level[3]. To efficiently harvest acoustic energy, sound needs to be focused and localized at the energy harvester location. For example, Helmholtz resonators with harvesters built into their cavity walls have been proposed to localize airflow energy with various configurations[4–7]. Another body of work also explored the harvesting of acoustic energy in hydraulic systems (in the form of a pressure ripple)[8], as well as the use of Helmholtz resonators again to enhance the pressure intensity[9]. Other forms of resonators, such as tube and quarter wave resonators, have been also used to harvest acoustic energy by combining them with piezoelectric diaphragms[10,11]. Acoustic/elastic phononic crystals (PCs) and metamaterials have been also proposed to enhance the performance of energy harvesters by focusing or localizing acoustic/elastic wave energy at the harvester location[12–15]. Other effort includes the use of metasurfaces by coiling up space for the confinement and enhanced harvesting of acoustic energy[16] as well as spatial grading to trap and harvest elastic wave energy[17].

Gradient index phononic crystals (GRIN-PCs)[18] have been suggested to construct various devices to guide and focus elastic waves for energy harvesting in plates[19,20].

They are constructed by gradually varying the unit cell properties in space to create a spatial refractive index gradient. GRIN-PCs have been also used to focus acoustic waves. Climente et al.[21] fabricated a 2D gradient index sonic crystal lens based on the hyperbolic secant profile to focus airborne sound. More recently, along with advancements in 3D printing technology, Xie et al.[22] succeeded in fabricating 2.5D and 3D Luneburg lenses capable of focusing acoustic waves in air. The circular/spherical (in 2D/3D) profile of Luneburg lens allows incident plane waves to be focused on the other side of the lens regardless of their direction. This was exploited[22] to enhance the performance of ultrasonic imaging using a 2.5D lens operating around 40 kHz; however, no numerical or experimental results were reported for the 3D Luneburg lens. Hyun et al.[23] designed a 2.5D GRIN-PC lens made of 3D-printed ABS cylinders to focus acoustic waves between 250 Hz and 1 kHz on an energy harvester with a peak enhancement observed in an acoustic duct system. For the focusing of underwater acoustic waves, Allam et al.[24] designed and experimentally validated a 3D GRIN-PC lens made of 3D-printed polymer.

In the present work, we design, analyze, and fabricate a GRIN-PC 3D lens to focus airborne audio frequency acoustic waves at a piezoelectric energy harvester in order to enhance the electrical power delivered to a resistive load. In the following, first, the PC unit cell structure and characteristics are discussed in detail highlighting the sources of anisotropy that arise from the geometry of the PC. A 3D GRIN-PC lens is then designed, simulated, 3D-printed, and experimentally validated. The factors affecting the lens performance are discussed with the aim of maximizing the amplitude of the acoustic pressure intensity at the focal spot. A piezoelectric energy harvester is then placed at the focal position of the lens and power enhancement by the lens is analyzed.

A simple cubic unit cell consisting of a 3D-printed

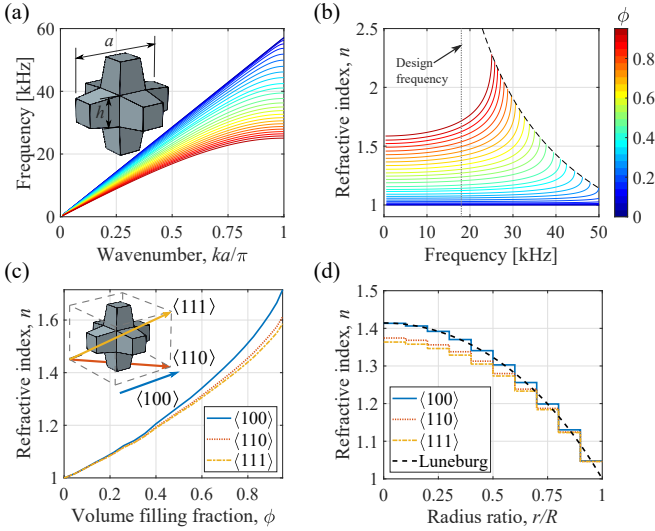[a)]Electronic mail: alper.erturk@me.gatech.edu; author to whom correspondence should be addressed

FIG. 1. (a) Dispersion plots of a unit cell in the main direction of wave propagation for different volume filling fraction values (ϕ), i.e. different polymer to cubic unit cell volume ratios. (b) Effective refractive index of the PC versus frequency for different ϕ values. (c) Effective refractive index at the design frequency (18 kHz) versus ϕ for different directions. (d) Analytical refractive index profile of an ideal Luneburg lens versus the discretized profile used in the implementation of the GRIN-PC lens for different directions. The effective refractive index in the diagonal $\langle 110 \rangle$ and $\langle 111 \rangle$ directions are also shown.

cross-shaped polymer structure in air is considered (inset of Fig. 1a) with a lattice size of $a = 3$ mm. The unit cell is based on the structure proposed by Xie et al.[22], but with tapered links to avoid sudden changes in the link cross-section between two neighboring cells. Comsol Multiphysics was used to construct an acoustic finite element model (FEM) for a single PC unit cell in order to obtain the dispersion curves as shown in Fig. 1a. Air was modeled as a periodic acoustic domain with a speed of sound $c_{air} = 343$ m/s and mass density $\rho_{air} = 1.14$ kg/m^3. Since the level of impedance mismatch between the polymer and air is several orders of magnitude, the polymer domain was assumed to be rigid, and was modeled as internal hard acoustic boundaries. The volume filling fraction of the unit cell is defined as $\phi = (3ah^2 - 2h^3)/a^3$, representing the volume of the polymer to the total volume of the cubic cell. The effective speed of sound $c_{eff} = 2\pi f/k$ can be controlled by changing the value of ϕ which changes the slope of the dispersion relation as shown in Fig. 1a, where f is the frequency in Hertz and k is the wavenumber. The effective refractive index of the unit cell, defined as $n = c_{air}/c_{eff}$, is shown in Fig. 1b. For a constant filling fraction, the effective refractive index of the material becomes more frequency dependent, i.e. less broadband, as the frequency increases (approaches the Bragg bandgap). The refractive index also becomes more frequency dependent as the filling fraction increases. A frequency of 18 kHz was se-

lected as a design frequency for the GRIN-PC lens, and the effective refractive index was plotted against the filling fraction in Fig. 1c. Note that, Fig. 1c is only valid at 18 kHz, but since the refractive index curve below this frequency is relatively flat for filling fractions of interest (below 0.7), it could be used to design broadband devices up to the design frequency. Fig. 1c could be used to construct a desired GRIN-PC refractive index profile by choosing the filling fraction corresponding to the desired refractive index value. To study the directional dependence of the PC, its effective refractive index was calculated in directions $\langle 100 \rangle$, $\langle 110 \rangle$, and $\langle 111 \rangle$ as shown in Fig. 1c. The specified directions were chosen since they represent extreme values with respect to the cubic symmetry of the lattice. As shown in Fig. 1c, the refractive index of the PC is anisotropic (at the design frequency), and the degree of anisotropy is proportional to the filling fraction. The anisotropy arises from the simple cubic periodicity of the unit cell, as well as its geometry. As the polymer volume in the unit cell increases, the geometry becomes comparable to the effective wavelength of the propagating acoustic waves, giving rise to increased anisotropy as shown in Fig. 1c.
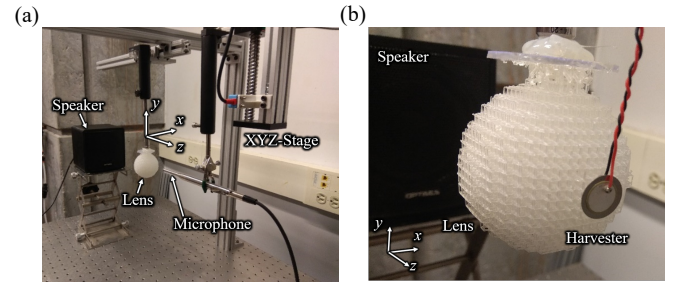

FIG. 2. Experimental setup (a) for measuring the acoustic pressure field of the 3D-printed GRIN-PC lens (microphone mounted on an XYZ stage scans the pressure field) and (b) for measuring the electrical power enhancement of a piezoelectric energy harvester placed at the focal spot of the GRIN-PC lens.

The refractive index profile in direction $\langle 100 \rangle$ was used to construct a GRIN-PC lens with the Luneburg profile given by $n(r) = \sqrt{2 - (r/R)^2}$, where r is the radial location inside the lens and R is the radius of the lens. The continuous analytical Luneburg profile as well as the discretized refractive index in the main lattice directions are shown in Fig. 1d. The refractive index slightly deviates from the analytical profile for the $\langle 110 \rangle$ and $\langle 111 \rangle$ directions which reduces the performance of the lens in these directions. The GRIN-PC lens is thus expected to be omindirectional, however with a slight variation in its performance depending on the direction. Moreover, this anisotropy could be further reduced by operating at lower frequencies or by using smaller unit cells.

The analytical profile was discretized for a unit cell of size $a = 3$ mm to construct a lens of radius $R = 30$ mm with 10 unit cells along the radius as shown in Fig. 2. The lens was constructed by using Fig. 1c to select the

required filling fraction at each unit cell, and the cross-sections of the links between each two neighboring cells were tapered to reduce the effect of discretization between the neighboring unit cells. On the wave propagation simulation side, a time domain acoustic FEM was constructed to simulate incident plane waves on the lens. The lens was modeled as hard boundary to an acoustic domain discretized with 7 elements per wavelength. The lens was ensonified with a plane Gaussian pulse centered at 18 kHz with 6 kHz bandwidth (BW), and the acoustic domain was surrounded with radiation boundaries to minimize wave reflections. A Courant-Friedrichs-Lewy (CFL) condition of 0.2 was used.

The designed lens was 3D printed using a Formlabs Form 2 stereolithography (SLA) 3D printer with a layer height of 100 μm and clear Formlabs resin. The scanning microphone setup, shown in Fig. 2a, was used to measure the pressure field behind the lens due to an incident plane wave. A speaker with frequency range of 1 - 22 kHz was excited with the same Gaussian pulse as in the numerical simulations. A 1/4" free field Larson Davis 2520 microphone was mounted on an automated XYZ stage to scan the pressure field at three perpendicular planes behind the lens. The grid cover of the microphone was removed to ensure that the pressure field could be measured as close as possible to the back surface of the lens. The microphone signal was digitized with a Handyscope HS3 oscilloscope, and a LABVIEW program was used to synchronize the excitation of the speaker with data acquisition. The received signal was time gated to avoid including any wall or other hard surfaces reflections in the measurement. The pressure field was measured once with the lens present, then with the lens removed to obtain the normalized pressure gain due to the presence of the lens. Subsequently, the lens was rotated to simulate plane waves incident from a different angle and the measurement was repeated.

The peak pressure field of the lens is shown in Fig. 3 at the focal spot of the lens with incident acoustic waves traveling in the positive z-direction (shown in Fig. 2a). A clear focal spot is observed behind the lens, and the experimentally measured focal spot size and shape is in good agreement with the numerical predictions. The pressure field at the center of the focal plane is shown in Fig. 4a. The experimental results show a narrower and lower amplitude at the focal spot than that predicted by the finite element simulations. The achieved gain is 6% lower than the predicted gain of 4.5 which is attributed to manufacturing tolerances of the 3D printing process as well as the directional pattern of the speaker. The results for $\langle 110 \rangle$ wave incidence show a reduction of 15% in the peak pressure amplitude compared to the $\langle 100 \rangle$. This reduction is attributed to the inherent anisotropy in the PC which caused a deviation from the exact Luneburg profile in this direction as shown in Fig. 1d.

The effect of changing the center frequency of the excitation was studied experimentally as shown in Fig. 4b. The figure shows that the lens can be used to focus in-
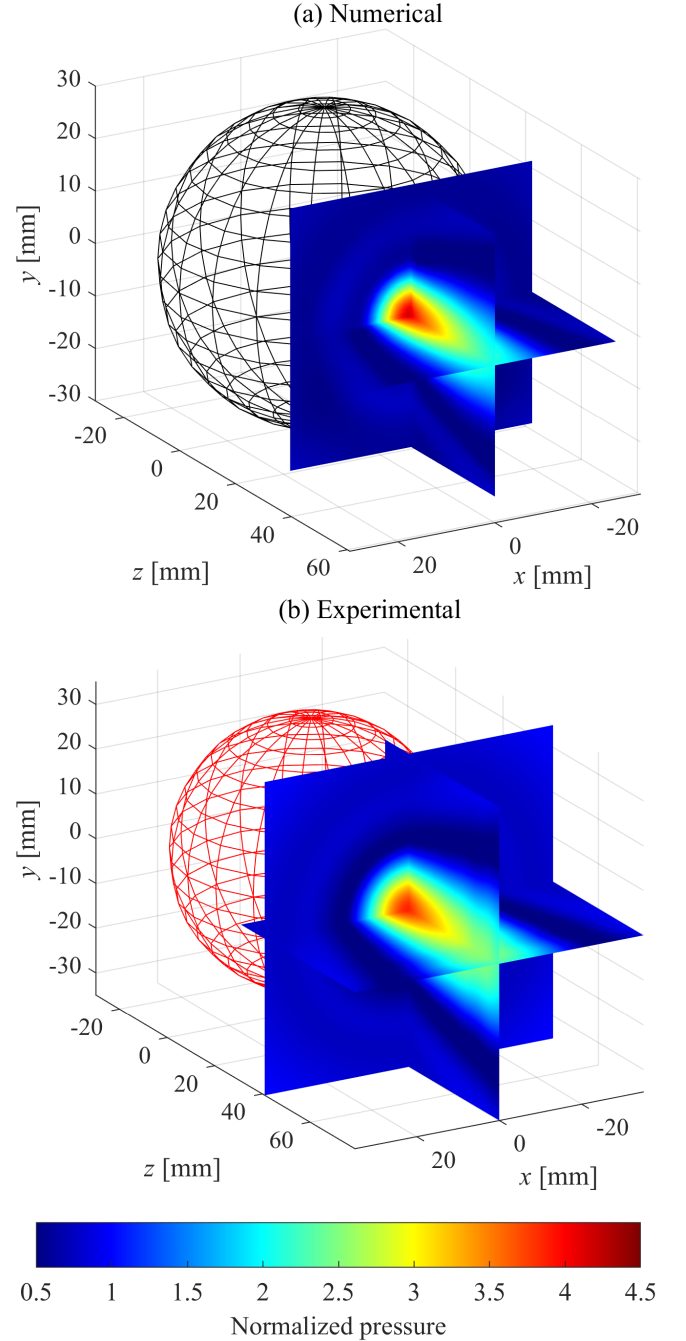

FIG. 3. Normalized peak pressure field behind the lens obtained (a) numerically and (b) experimentally.

cident waves from frequencies lower than 10 kHz to frequencies higher than 20 kHz. However, more focusing is observed at higher frequencies, since the lens is diffraction limited. Fig. 4c shows the experimental pressure time series at the focal position of the lens compared to the baseline case (in the absence of the lens). At the target design frequency (18 kHz), a pressure gain of 4.2 was observed in both the peak and RMS pressures at the focal positions. This corresponds to an increase in acoustic
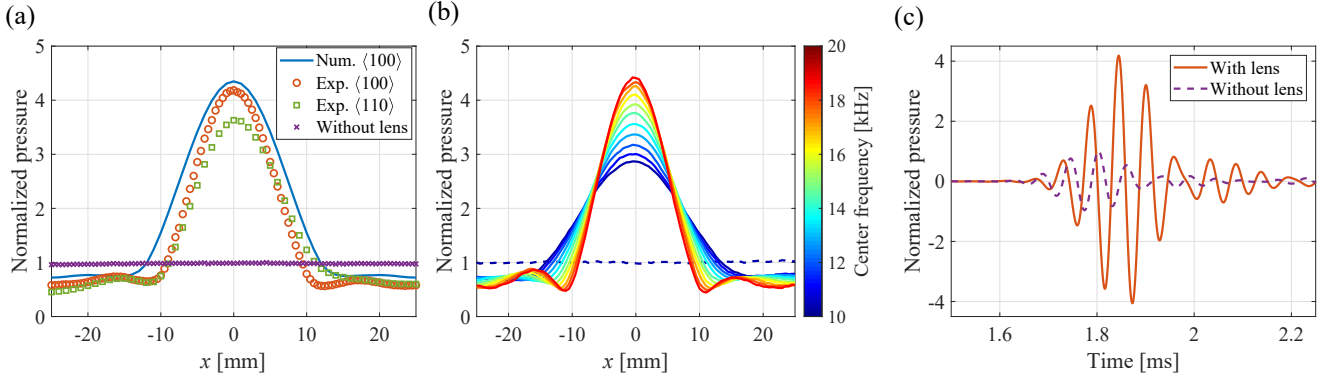
FIG. 4. (a) Normalized pressure at the focal plane obtained numerically and experimentally. The experimental pressure fields are shown for waves propagating in the directions ⟨110⟩ and ⟨100⟩ with respect to the PC lattice. (b) Normalized peak pressure obtained experimentally for different Gaussian pulse center frequencies. The bandwidth was kept constant at 6 kHz. (c) Time series for the pressure at the focal position of the lens compared to its absence. The case shown is for a pulse with 18 kHz center frequency.

intensity (power) at the focal spot by a factor of 17.6. The pressure gain of the lens could be further improved by increasing the lens aperture (size) allowing for more energy to be directed toward the focal spot. However, this is typically bounded by the size limitations of the 3D printing process as well as the space available for the lens (to keep it compact in a given application).

To demonstrate the ability of the 3D GRIN-PC lens for enhanced sound energy harvesting, a piezoelectric energy harvester was placed at the focal spot of the lens as shown in Fig. 2b. The harvester was selected to operate near the center of the lens design frequency bandwidth around 15 kHz. It is a circular unimorph with an outer diameter of 13.5 mm with a substrate layer of thickness 0.2 mm made of stainless steel and a piezoelectric layer of thickness 0.15 mm and diameter 10 mm made of PZT-4. The mechanical quality factor of the harvester is $Q_m = 50$. To predict the dynamics of the harvester, a frequency domain piezoelectric FEM was constructed. An axisymmetric FEM of the harvester was subjected to a uniform harmonic pressure of 30 Pa (≈ 120 dB, reference pressure: 20 µPa) and the output electrical power across different load resistance values was obtained in Fig. 5. Two power peaks at 14.5 kHz and 15.5 kHz are observed representing the short and open-circuit resonance frequencies of the harvester. The output power is larger for resistance values closer to the open-circuit resonance (around 30 kΩ); however, the frequency bandwidth is narrower compared to the bandwidth of resistor values between 1 kΩ and 10 kΩ.

The experimental setup shown in Fig. 2b was used to measure the output power enhancement by the lens. The lens-harvester system was excited with a modulated Gaussian pulse generated through a loud speaker. Three different pulses were used: the first pulse was centered around 15 kHz and had a bandwidth of 4 kHz which is much larger than the bandwidth of the harvester (around 500 Hz as shown in Fig. 5). Additionally, two narrow

band pulses (500 Hz bandwidth) centered around 14.5 kHz and 15 kHz were chosen to target the bandwidth of the harvester. The amplitude of the incident acoustic wave was kept constant for all pulses, and was set to 30 Pa ($\approx$120 dB) measured at the harvester location in the absence of the lens. A variable load resistor was connected to the harvester via two thin wires which were also used to suspend the harvester to emulate free boundary conditions. The voltage generated across the load resistor was measured and used to calculate the output power of the harvester at different resistance values. The lens was then removed and the output power of the harvester was measured again as a baseline to determine the power enhancement due to the presence of the lens.
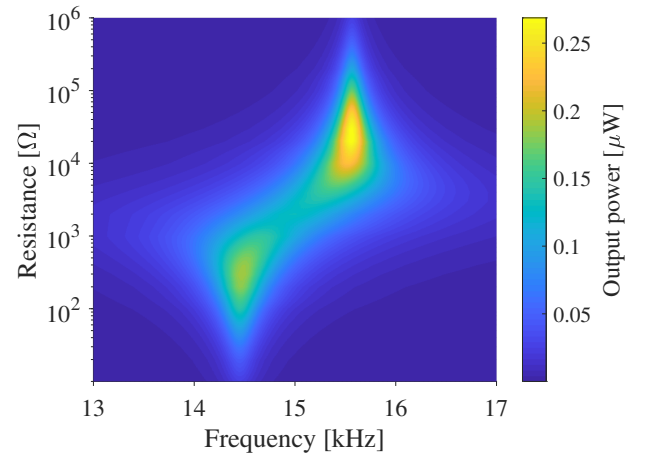

FIG. 5. Simulated output power of the harvester when subjected to a uniform harmonic pressure of 30 Pa ($\approx$120 dB). The power is plotted vs excitation frequency and load resistance.

The peak power generated for different resistor values and pulses of different center frequency and bandwidth is summarized in Fig. 6a. Clearly, the presence of the lens

increases the electrical power delivered to the load by an order of magnitude as compared to the respective baseline case without the lens. The electrical power gain is slightly lower than the acoustic power gain [cf. Fig.4(b) squared] since the dimensions of the energy harvester are larger than the focal spot of the lens at these frequencies (i.e. the harvester was not optimized). For all resistance values, the electrical power output for the wideband pulse was lower than the narrowband pulses, which is expected, since the bandwidth of the harvester is limited to a narrow band of approximately 500 Hz as shown in Fig. 5. A narrow-band pulse centered at 14.5 kHz (close to the short-circuit resonance frequency) generated more electrical power at lower resistor values (closer to optimal short-circuit resonance load as expected[25]) compared to the 15 kHz pulse. A maximum power output of 1.2 µW was observed for the 15 kHz pulse at a load resistance of 6 kΩ which is close to the optimal resistance value for the energy harvester. The voltage time series for this case is shown in Fig. 6b. It should be noted that the bandwidth of the lens-harvester system is mainly limited by that of the harvester in this case, which can be further improved by using an energy harvester with larger bandwidth, such as those exploiting designed nonlinearities[26]. Moreover, the lens was designed for a peak performance near 18 kHz, while the harvester was chosen to operate around 15 kHz. It is possible to achieve a slightly better performance if the lens was designed at the same center frequency as the energy harvester (i.e. 15 kHz), however at the expense of reduced performance at higher frequencies.

To conclude, a gradient-index phononic crystal lens was designed for audio frequency acoustic waves and employed to enhance the electrical power of a piezoelectric energy harvester placed at its focal position. Pressure field measurements of the designed lens revealed its ability to focus acoustic power over a broad frequency range between 10-20 kHz, with acoustic power gain levels as high as 17.6 fold. As a result, the use of the lens in sound energy harvesting enhanced the power delivered to the load by more than an order of magnitude as compared to the baseline case (without the lens). The lens-harvester system was able to generate 1.2 µW of electric power from 120 dB airborne sound, which is well above most sound energy harvester designs with similar scale that produce nano-Watt level power.

The data that support the findings of this study are available from the corresponding author upon reasonable request.
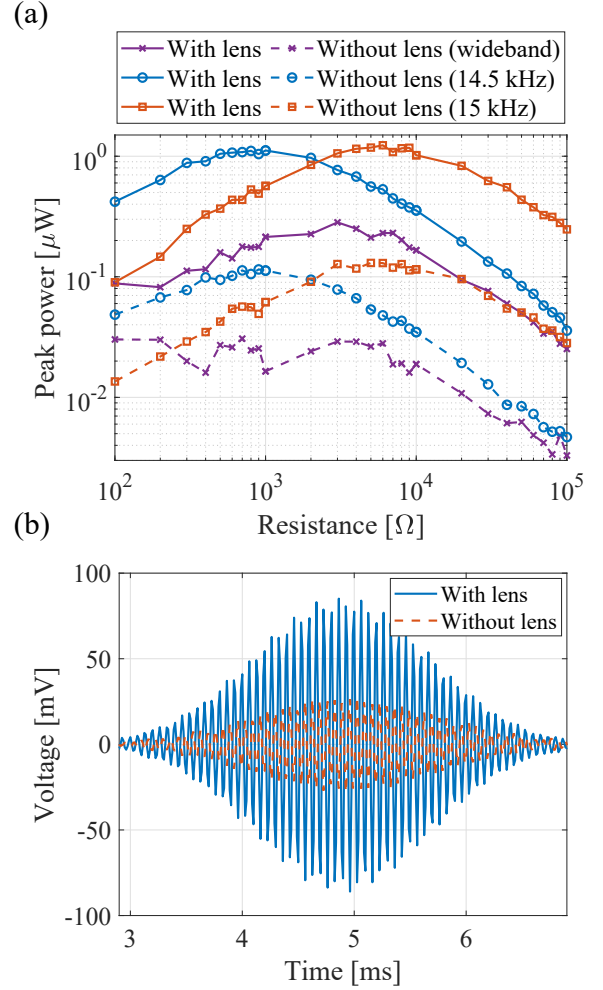
(a)

(b)

FIG. 6. (a) Experimental peak harvested electrical power versus load resistance for an incident acoustic plane wave with a peak pressure of 30 Pa (≈120 dB) on the lens-harvester system. The output power from a pulse with center frequency f_c= 15 kHz and bandwidth BW=4 kHz (wideband) is compared to pulses with narrower bandwidth (BW=500 Hz) and centered around f_c= 14.5 kHz and f_c= 15 kHz. The baseline case for the harvester without the lens is also shown for all the pulse shapes considered. (b) The voltage time series obtained experimentally for the maximum power output obtained with a pulse centered at f_c= 15 kHz with BW=500 Hz and a load resistance of R_l=6 kΩ connected to the harvester.

[1] F. U. Khan and Izhar, J. Micromech. Microeng. **25**, 023001 (2015).
[2] M. Yuan, Z. Cao, J. Luo, and X. Chou, Micromachines **10**, 48 (2019).
[3] J. Choi, I. Jung, and C.-Y. Kang, Nano Energy **56**, 169 (2019).
[4] S. B. Horowitz, M. Sheplak, L. N. Cattafesta, and T. Nishida, J. Micromech. Microeng. **16**, S174 (2006).
[5] F. Liu, A. Phipps, S. Horowitz, K. Ngo, L. Cattafesta, T. Nishida, and M. Sheplak, J. Acoust. Soc. Am. **123**, 1983 (2008).
[6] M. Yuan, Z. Cao, J. Luo, J. Zhang, and C. Chang, Sens. Actuators, A **264**, 84 (2017).
[7] G.-S. Liu, Y.-Y. Peng, M.-H. Liu, X.-Y. Zou, and J.-C. Cheng, Appl. Phys. Lett. **113**, 153503 (2018).
[8] E. Skow, K. Cunefare, and A. Erturk, Smart materials and structures **23**, 104011 (2014).
[9] F. J. Schwartz, E. A. Skow, A. Erturk, and K. A. Cunefare, in *Sensors and Smart Structures Technologies for Civil, Mechanical, and Aerospace Systems 2017*, Vol. 10168 (International Society for Optics and Photonics, 2017) p. 1016824.
[10] B. Li, J. H. You, and Y.-J. Kim, Smart Mater. Struct. **22**, 055013 (2013).
[11] H. Guo, Y. Wang, X. Wang, and C. Xu, Advances in Mechanical Engineering **10**, 1687814017748077 (2018).

[12] L.-Y. Wu, L.-W. Chen, and C.-M. Liu, Appl. Phys. Lett. **95**, 013506 (2009).

[13] W.-C. Wang, L.-Y. Wu, L.-W. Chen, and C.-M. Liu, Smart Mater. Struct. **19**, 045016 (2010).

[14] M. Carrara, M. R. Cacan, J. Toussaint, M. J. Leamy, M. Ruzzene, and A. Erturk, Smart Mater. Struct. **22**, 065004 (2013).

[15] A. Yang, P. Li, Y. Wen, C. Lu, X. Peng, J. Zhang, and W. He, Appl. Phys. Express **6**, 127101 (2013).

[16] S. Qi and B. Assouar, Appl. Phys. Lett. **111**, 243506 (2017).

[17] J. M. De Ponti, A. Colombi, R. Ardito, F. Braghin, A. Corigliano, and R. V. Craster, New Journal of Physics **22**, 013013 (2020).

[18] Y. Jin, B. Djafari-Rouhani, and D. Torrent, Nanophotonics **8**, 685 (2019).

[19] S. Tol, F. L. Degertekin, and A. Erturk, Appl. Phys. Lett. **111**, 013503 (2017).

[20] S. Tol, F. Degertekin, and A. Erturk, Addit. Manuf. **29**, 100780 (2019).

[21] A. Climente, D. Torrent, and J. Sánchez-Dehesa, Appl. Phys. Lett. **97**, 104103 (2010).

[22] Y. Xie, Y. Fu, Z. Jia, J. Li, C. Shen, Y. Xu, H. Chen, and S. A. Cummer, Sci. Rep. **8**, 16188 (2018).

[23] J. Hyun, C.-S. Park, J. Chang, W.-H. Cho, and M. Kim, Appl. Phys. Lett. **116**, 234101 (2020).

[24] A. Allam, K. Sabra, and A. Erturk, Phys. Rev. Applied **13**, 064064 (2020).

[25] A. Erturk and D. J. Inman, *Piezoelectric energy harvesting* (John Wiley & Sons, 2011).

[26] M. F. Daqaq, R. Masana, A. Erturk, and D. Dane Quinn, Applied Mechanics Reviews **66** (2014).